ESI:

Value Modeling:

The value of an energy storage system is expected to increase greatly in the future, especially as low-cost variable renewable energy begins to become available and in excess of demand. However, to evaluate the merits of energy storage technologies, the value is estimated from current market conditions, where the two markets unlikely to be saturated are capacity payments and arbitrage[3]. Here, arbitrage value is defined as the summation of the annual revenue that could be earned by a device, minus the cost to purchase energy at off-peak times[4].

The revenue from capacity payments (CP) is highly variable, mainly because these payments are used to incentivize new generation capacity, and are therefore low in markets with excess capacity, and high in markets short on capacity[24]. Thus, instead of taking an average of actual CPs, which range \$0-500/kW-yr[3], a more fundamental method is used to estimate the CP that one could expect to earn. That is, the reason a CP is offered in the first place is that in regulated markets, grid resources that only operate during peak times, namely peaking gas turbines, do not earn enough revenue from energy sales to be profitable. Then, logically, a CP is expected to be the subsidy needed to allow a balancing resource to have zero NPV. This is exactly what the net cost of new entry (Net CONE)[42] parameter represents, and it is widely reported. This cost is calculated as the total cost of a resource, minus the revenue it earns from energy sales and other ancillary revenues. Thus, it is this net loss that needs to be compensated by a CP. Here, this value is estimated to be \$95/kW-yr based on the 2018 average Net CONE in the PJM market[23].

Multijunction Photovoltaics (MPV)

Additional Losses - Resistive and shadowing loss:

Practical PV cells are subject to a voltage loss due to series resistance. At the several hundred kW/m^2 power densities of light incident on the PV cells envisioned herein, the cell's output current density would be well above 10 A/cm^2, high enough to require effective mitigation strategies for the series resistance losses. Such current densities are comparable to those encountered in high-concentration solar CPV, and the same mitigation strategies are applicable, centering on the use of properly engineered front-contact grids to reduce the main source of series resistance in III-V PV cells. The metal-semiconductor interface is critical to a low contact resistance, and care must be taken to choose metals with an appropriate work function in order to achieve ohmic behavior. The individual grids must have sufficient cross-section to mitigate Joule losses from the high currents being transported, but without excessively shadowing the semiconductor. In general, raising the grid coverage lowers the series resistance loss at the expense of raising the shadowing loss, and an optimal tradeoff in grid coverage must be found to balance these two competing losses.

Using a well-established lumped-resistance model[43], we can make a reliable estimate of these losses based on experimentally validated cell and grid parameters. For the 1.4 eV / 1.2 eV two-junction cell design under the 2100°C spectrum, the photon flux above the 1.2 eV bandgap corresponds to a current density of 14 A/cm^2. This current density is shared between the two

junctions[44] so the net current density through the device is 7 A/cm^2. Because resistive power losses are proportional to the square of the current density, this sharing of current density between junctions is one of the significant practical benefits of multijunction cells at high incident fluxes such as the TPV application discussed here. The main sources of series resistance loss in high-performance III-V multijunction devices is due to the lateral current flow in the top-junction emitter; the contact resistivity between the emitter and the grid fingers; and the current flow through the grid fingers. The loss in the emitter is proportional to the emitter sheet resistivities of the top junction, and we have demonstrated very low ~30 ohm/sq resistivities for this junction. Assuming that value for the emitter resistivity; grid parameters readily achieved by conventional photolithographic metallization; and the use of well-established methods to minimize the finger length[45], we estimate that a very acceptable series resistance plus grid shadowing loss of 3% relative (i.e., 3% of the cell efficiency – a loss of 1.3% absolute for a nominally 45% efficient cell) is readily achievable entirely with well-established device metallization techniques. Importantly, for this MPV application, this tradeoff may be much less demanding than for CPV, because many of the photons blocked from entering the cell by the front grids will be reflected back to the thermal emitter so that their energy can be reused.

Manufacturing Approach

As described in detail in Geisz, *et. al.*[39], in the inverted metamorphic multijunction (IMM) architecture the top junction is grown first, followed by the bottom junction, which leaves the back contact layer accessible for fabrication of a high reflectivity BSR; the two junctions are separated by an Esaki tunnel junction. Such tunnel junctions are well established as an extremely high-performance, low-loss interconnect for III-V photovoltaic junctions at current densities up to and beyond the current densities of interest in the present application[46-50]. The device is then bonded to a handle and the substrate removed. As shown in Extended Data Figure 1, 1.0-eV $Ga_{0.7}In_{0.3}As$ is lattice-mismatched with respect to the GaAs substrate, with ~2.1% larger lattice constant, and has already been demonstrated to be a successful high quality third junction in high efficiency four-junction solar cells [51], with a voltage penalty $W_{oc} < 0.4$ V. Illustrated in Extended Data Figure 1B, the mismatched cell is fabricated by first growing a compositionally step-graded buffer layer (CGB) that incrementally increases the lattice constant and relieves the accumulating strain[52], leading to a mismatched cell with a low threading dislocation density., The CGB approach has been put on a firm scientific foundation[53,54], and had been demonstrated to enable III-V semiconductor-alloy junctions with extremely high photovoltaic-device quality over a very wide range of bandgaps[52,55-58]. For application in solar cells, the CGB must be transparent to light below the top junction bandgap[52,55-58]. However, for the present TPV application, returning sub-bandgap photons to the source is crucial for TPV system efficiency, so free carrier absorption in the CGB layers would be problematic. Therefore, here we envision growing a tandem cell by adding a 1.2-eV $Al_{0.15}Ga_{0.55}In_{0.3}As$ above the GaInAs cell, at the same mismatched lattice constant, and then completely removing the CGB during processing. The resulting two-junction device would be thin, mounted to a stable handle and have a high reflectivity BSR. Variations on this design are also possible to achieve other band gap combinations as well, and it is through this new design of a MPV that the TEGS-MPV concept can achieve $\geq$ 50% RTE.

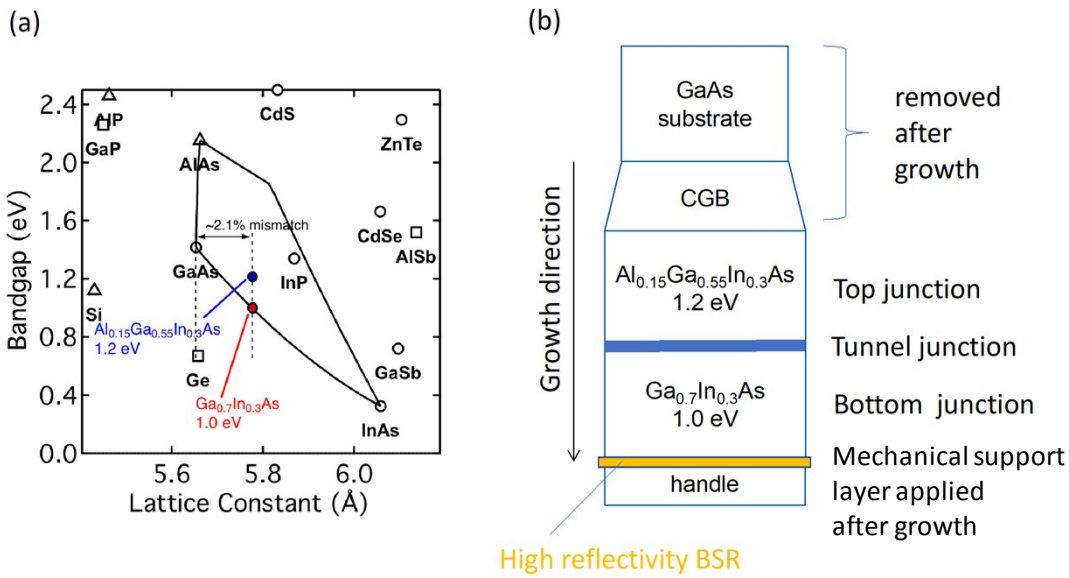

Extended Data Figure 1A: (a) Bandgaps and lattice constants of the common III-V binary and ternary compounds. The 1.2 and 1.0 eV alloys are indicated. (b) Schematic of the proposed cell design. The substrate and CGB layers would be removed during processing, leaving a thin two-junction device with a high reflectivity BSR.

Radiative Heat Transfer in Optical Cavity

In this section, we quantify how the emitter to MPV cell surface area ratio ($A_{emitter}/A_{cell}$) changes the incident flux of light on the MPV cell. This is of interest because tungsten (W), which is needed to prevent evaporation of the emitter material, has an emissivity significantly below a blackbody. In a design where the emitter and MPV have equal amount of area, this would yield a significant penalty on the output power density, which would translate to corresponding penalties on the efficiency and cost. We used Monte Carlo Ray Tracing (MCRT) to study radiative heat transfer based on Howell and Siegel[59] and Haji-Sheikh and Howell[55]. To increase $A_{emitter}/A_{cell}$, we consider W foil fins attached to W foil plates that cover graphite pipes and therefore serve as the emitter. For simplicity, the calculation assumes the MPV cell has BSR reflectivity of 0.98 for photons with energy below the bandgap. The reflectivity of the MPV cell for photons with energy above the bandgap is assumed to be zero. The W emitter is assumed to be at 2100°C while the cell temperature is assumed to be 25°C. The spectral reflectivity of W is taken from the experimental data of Coblentz[40]. The distance between adjacent fins (D) and the total number of fins on each planer face of the emitter are assumed to be 2 cm and 8, respectively. These two parameters are kept fixed in the simulation while the length of fins (L_{fin}) and the size of MPV cells (L_{cell}) are changed from 8 cm to 14 cm and 0 to 2.8 cm, respectively to achieve different $A_{emitter}/A_{cell}$ ratios.

In the MCRT model, the number of computational cells on the surface of the optical cavity is controlled to contain roughly the same number of particles and consequently similar statistical variation. It was found that around 50 particles per computational cell on average is enough to resolve radiation field on the MPV cells and W emitter. Furthermore, the effect of the number of particles in the optical cavity was found that roughly 200,000 – 450,000 particles are sufficient to capture the radiation distribution on the surfaces of optical cavity.

The effect of the $A_{emitter}/A_{cell}$ ratio on the incident radiative power above the bandgap for two different bandgaps (Eg), i.e., 1.43 eV and 1 eV is shown in Extended Data Figure 2. As expected, increasing $A_{emitter}/A_{cell}$ enhances the above bandgap incident power onto the cells. For example, with Eg =1.43 eV and $A_{emitter}/A_{cell}$, power density is 1.6 times the base case. This effect is important, since the increase in power density is what enables the efficiency to be high ≥ 50%.

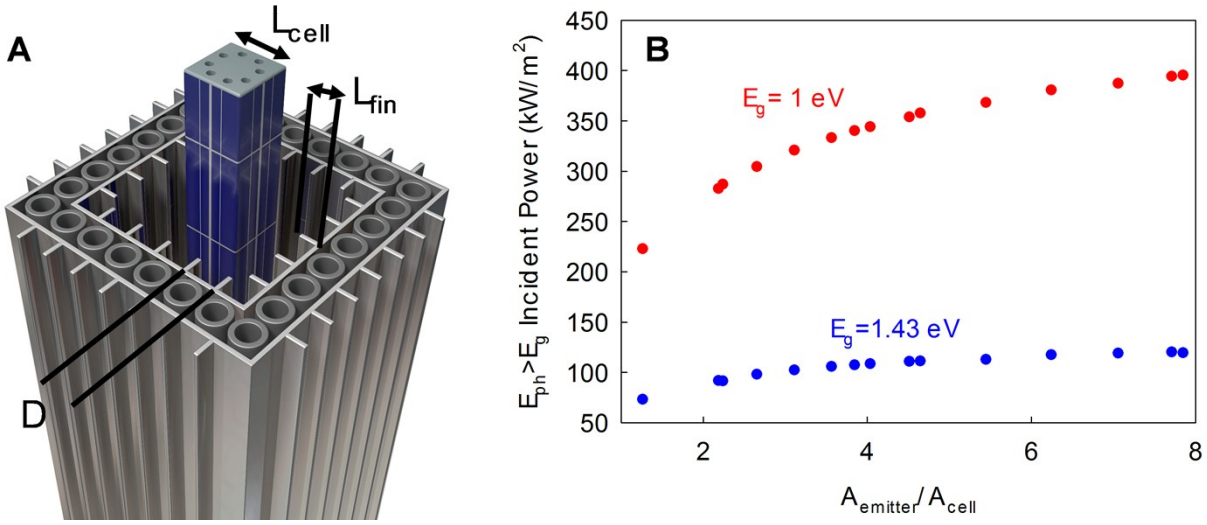

Extended Data Figure 2: A – Illustration of an individual power block sub-unit identifying the characteristic lengths used in the MCRT calculations. **B–** The effect of $A_{emitter}/A_{cell}$ on above bandgap incident radiative power.

Convective Heat loss

Here, we analyze the convective heat loss from the emitter to the MPV cells as a step towards determining the efficiency of the power block. It is not clear *a priori*, if the convective heat loss from the emitter is sufficiently low to enable to high power output. Second, as W fins will be employed to increase the emitter effective emissivity, these fins may enhance the convective heat loss from the emitter, potentially negating the gains. If the use of W fins causes significant convective heat loss, then increasing the radiative power due to enhancement in emitter surface area may not be very effective overall. In this section, we describe a 3D steady-state fluid and heat transfer model for evaluating the convective heat loss.

The computational domain consists of planer W surfaces emitter with W fins and MPV cells. The total vertical height of the system and the distance between the fins are 2 m and 2 cm, respectively. The emitter temperature is assumed to be 2100°C while the MPV cell temperature is 25°C. The gas in between the W and MPV cells is taken as 1 atm krypton (Kr), with temperature dependent viscosity, thermal conductivity, and density. The flow is assumed to be Newtonian, viscous and compressible. The governing equations are as follows,

Continuity equation:

$$\frac{\partial(\rho u)}{\partial x}+\frac{\partial(\rho v)}{\partial y}+\frac{\partial(\rho w)}{\partial z}=0 \qquad (1)$$

Momentum Equations:

$$\frac{\partial\left(\rho u^2\right)}{\partial x}+\frac{\partial\left(\rho uv\right)}{\partial y}+\frac{\partial\left(\rho uw\right)}{\partial z}=-\frac{\partial P}{\partial x}+\mu\left(\frac{\partial^2 u}{\partial^2 x}+\frac{\partial^2 u}{\partial^2 y}+\frac{\partial^2 u}{\partial^2 z}\right) \tag{2}$$

$$\frac{\partial\left(\rho vu\right)}{\partial x}+\frac{\partial\left(\rho v^2\right)}{\partial y}+\frac{\partial\left(\rho vw\right)}{\partial z}=-\frac{\partial P}{\partial y}+\mu\left(\frac{\partial^2 v}{\partial^2 x}+\frac{\partial^2 v}{\partial^2 y}+\frac{\partial^2 v}{\partial^2 z}\right)+g\left(\rho-\rho_a\right) \tag{3}$$

$$\frac{\partial\left(\rho wu\right)}{\partial x}+\frac{\partial\left(\rho wv\right)}{\partial y}+\frac{\partial\left(\rho w^2\right)}{\partial z}=-\frac{\partial P}{\partial z}+\mu\left(\frac{\partial^2 w}{\partial^2 x}+\frac{\partial^2 w}{\partial^2 y}+\frac{\partial^2 w}{\partial^2 z}\right) \tag{4}$$

Energy Equation:

$$\frac{\partial\left(\rho C_p uT\right)}{\partial x}+\frac{\partial\left(\rho C_p vT\right)}{\partial y}+\frac{\partial\left(\rho C_p wT\right)}{\partial z}=k\left(\frac{\partial^2 T}{\partial^2 x}+\frac{\partial^2 T}{\partial^2 y}+\frac{\partial^2 T}{\partial^2 z}\right)+\mu\Phi \tag{5}$$

where u, v, w are the fluid velocity components, ρ is density, P is pressure, μ is dynamic viscosity, C_p is the specific heat capacity, T is temperature, and Φ is viscous dissipation. The density of Kr is calculated from the ideal gas law below, where M_w is the molar mass of Kr and R is ideal gas constant.

$$\rho=\frac{P}{\left(R/M_w\right)T} \tag{6}$$

To reduce computational cost, only one quadrant is modeled. At the symmetry surfaces, the gradient of all variables is set to zero. The numerical simulation was conducted using ANSYS Icepak, a commercially available CFD code based on the finite volume method. The governing equations are discretized by applying a finite volume method in which conservation laws are applied over finite-sized control volumes around grid points, and the governing equations are then integrated over the volume. The QUICK scheme was used to discretize convection/diffusion terms in momentum and energy equations. The numerical simulation is accomplished by using the SIMPLE algorithm. In this technique, using a guessed pressure and velocity field, they are first calculated from the Navier–Stokes equations. Then, to satisfy the continuity equation, the pressure and velocities are corrected. The numerical solution is regarded as convergent at an iteration in which the summation of absolute values of relative errors in temperature, velocity components and pressure reach 10^{-9}, 10^{-6} and 10^{-4}, respectively. Convergence with respect to the number of grids in the computational domain is carefully checked and a fine grid is used in the regions of the boundary layers where the gradients of velocity and temperatures are steeper.

Two main factors influence the heat loss from the emitter: (i) the surface area of the emitter and W fins in contact with the gas, and (ii) the flow pattern and thermal boundary layer thickness near the hot emitter surfaces. Intuitively, larger emitter surface area and closer distance between MPV cells and the emitter result in more heat loss, but it is not clear a *priori* how the size of W fins and MPV cell changes the flow pattern in the optical cavity and consequently the convective

heat transfer near the hot surfaces. The effect of normalized fin length (L_{fin}/D) and MPV cells dimension (L_{cell}/D) on overall heat loss from the emitter is shown in Extended Data Figure 3B. The dimensions are normalized with respect to fin spacing (D). Counterintuitively, increasing the length of W fins decreases the heat loss from the emitter. This is because the convective enhancement of heat transfer near the surfaces reduces, while the change in the conductive heat contribution is minimal. As can be seen from temperature distribution in a plane 20 cm from the base of the system (Extended Data Figure 3A), for larger L_{fin}/D, the high temperature and low velocity hot gas becomes trapped between two adjacent fins causing a thicker thermal boundary layer near the hot surfaces to develop and consequently lower heat loss compared the case with small L_{fin}/D. The effect of L_{cell}/D on heat loss is also shown in Extended Data Figure 3A. As seen by decreasing the MPV cell size, the heat loss decreases which is mainly due to a diminishing conductive contribution for larger cell-emitter distances. Evidently, for small distances between the emitter and cell the heat loss is dominated by the conduction and fluid circulation due to natural convection is insignificant. This is shown in the temperature contours of Extended Data Figure 3A as the thickness of thermal boundary layer doesn't change significantly by changing the size of MPV cells. In conclusion, the analysis suggests (i) the convective e heat loss from the system is about 5 kW/m^2 or less, when normalized by the cell area and (ii) increasing the emitter to cell area ratio not only enhances the radiative power incident onto the MPV cells but it also helps to minimize the convective heat losses by trapping hot gas between fins creating stagnant zones. Therefore, the addition of W fins has a significant performance advantage.

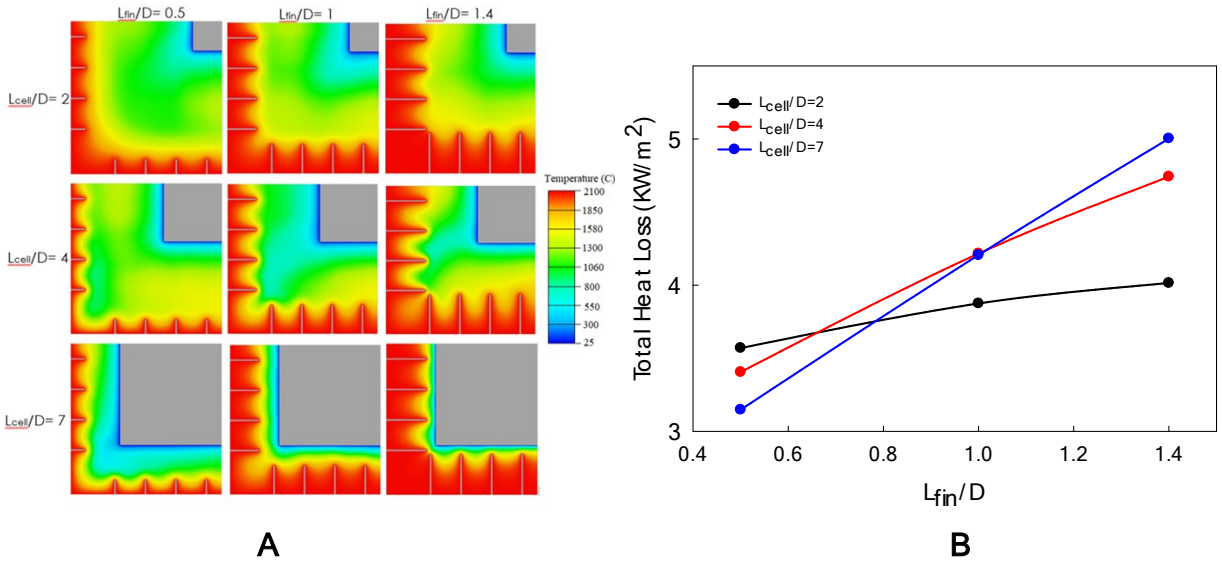

Extended Data Figure 3: A – Temperature distribution in a plane 20 cm from the base of the system **B –** effect of size of W fins and MPV cell on heat loss

Cell Temperature Regulation

The MPV concept proposed requires the photovoltaic cells to be located in close proximity (a few cm) to an emitter surface as hot as 2400°C. This presents an extreme, but manageable thermal situation to maintain the MPV cell at low temperature (i.e., below 40°C) which is vital to efficiency and cell survival. Fundamentally, for the cell to be ~10°C above the cooling water temperature while the emitter is at 2400°C, the thermal resistance between cell and the bulk

cooling water must be ~100 times less than the resistance between the emitter and cell. This can be achieved with turbulent convection in small extruded channels near the surface with negligible (but included) pumping power consumption from dry-cooled water as shown in Extended Data Figure 4. The cost impact of this cooling is significant and discussed in the next section.

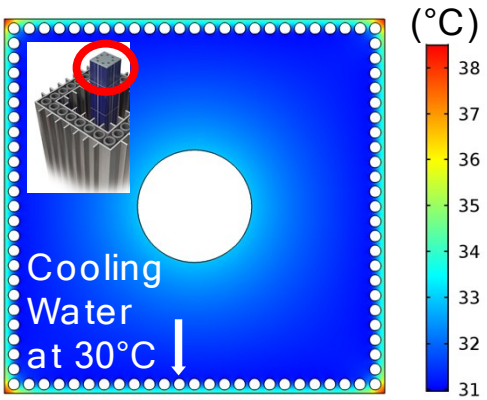

Extended Data Figure 4 : Cross-section view looking down of COMSOL simulation of MPV Cooling block. 112 kW/m^2 heat flux is applied to the MPV surfaces (4 edges). With a water flow rate of 3 m/s and inlet temperature of 30°C (from a dry cooler), the MPV surface remains below 35°C. This is achieved with low pumping power of 250W/m^2. The dominant (~4X) pumping power is required to reject this heat in the dry cooler. The water returns through the large center channel which does not contribute significantly to the heat transfer.

Techno-Economic Modeling

The full-scale size is selected to approach the asymptotic minimum cost, while remaining at a scale that could be reasonably manufactured (1 GWh-e), as shown in Extended Data Figure 5. The system consists of two tanks of the same volume and wall thickness, with only one filled, and less insulation for the colder tank. The system is designed to have 10 hours of storage, with equal charging (resistive heating) and discharging (MPV power cycle) rates of 100 MW-e. A full-scale model of this system is presented in Extended Data Figure 6, with tanks of ~15 m diameter.

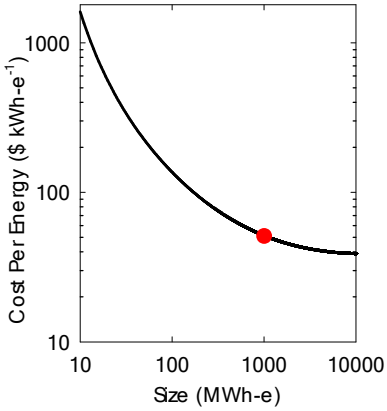

Extended Data Figure 5: Scaling tradeoff between cost and size for TEGS CPE components.

Tanks

The material in direct contact with Si, providing mechanical and chemical containment, is made from isostatic graphite at a typical quoted cost for large quantities of $7/kg. This graphite grade has multiple trade names, such as KYM-20, AS-TJ, AR-06, and G330. The common features are a density greater than 1.750 g/cm^3, with particle and pore size below 50 μm. These large tanks can be built in sections as shown in Extended Data Figure 6D, approximately one meter in size. The tank has two layers, which reduce the likelihood of leaks. The units are connected by flanges on all edges with high strength (120 MPa fracture under tensile loading) carbon fiber composite (CFC) threaded rod and nuts, as shown in Extended Data Figure 7B. Since these CFC fasteners are exposed to Si, an experiment was conducted (1800°C for 120 minutes) to determine their behavior in contact with Si. As shown in Extended Data Figure 7C, similar to the bulk graphite tank, the threaded rod developed a SiC protective layer that prevented further reaction, and the material retained its mechanical integrity. Sealing is achieved using a thin grafoil gasket described in the following proof of concept experiments.

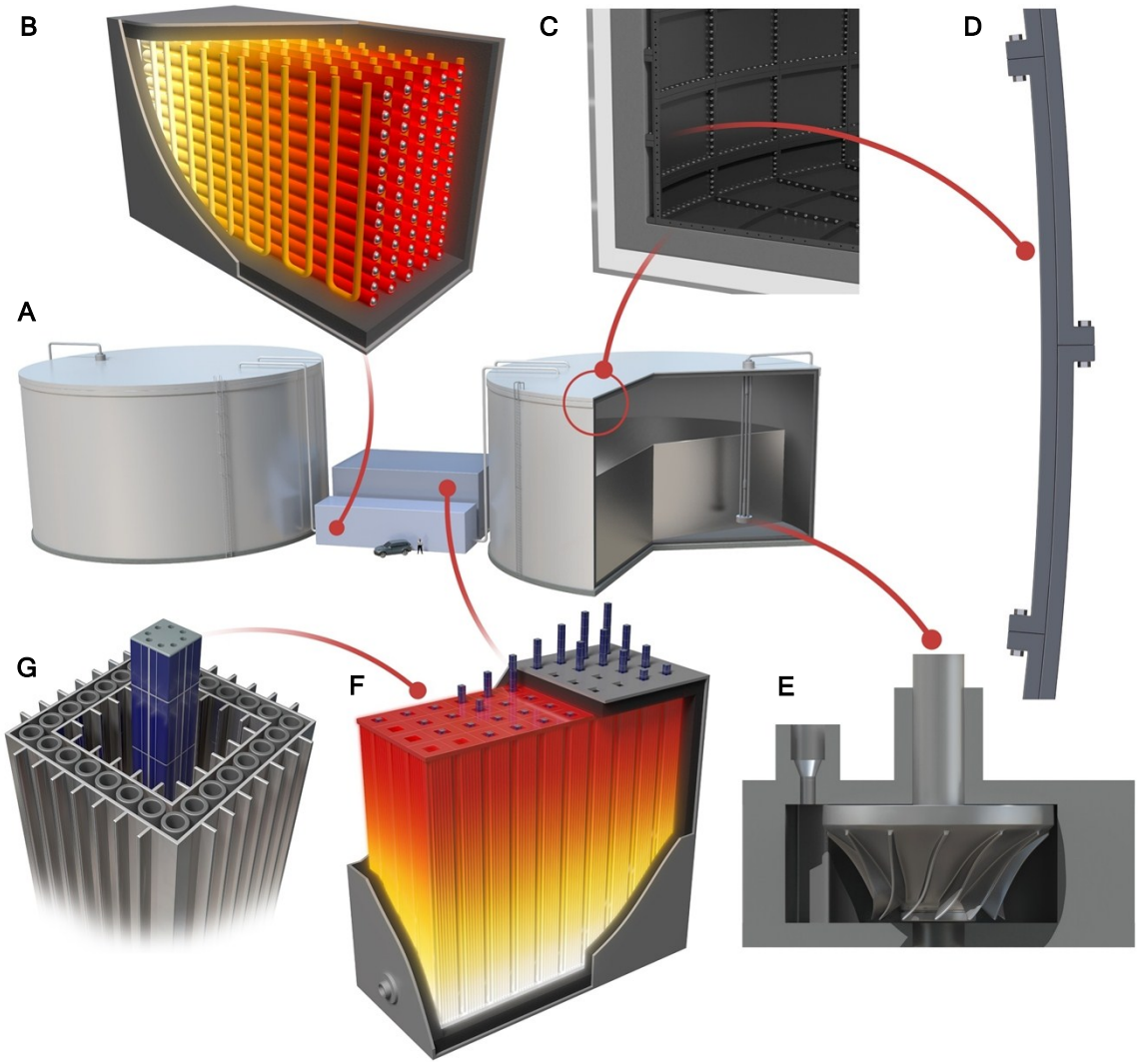

Extended Data Figure 6A – TEGS-MPV system concept consisting of a hot and cold tank, MPV heat engine (**F**), and resistive heating charger (**B**). System shown stores 1 GWh-e, with human and car shown for scale. **B** – Heater, showing horizontal graphite pipes which connect to headers and vertical graphite rods for resistive heating. **C** – Graphite tank showing section and insulation design. **D** – Tank sections and bolting scheme using two layers. **E** – Representative graphite centrifugal pump to transport silicon to the heater and heat engine. **F** – Heat engine with vertically actuated MPV arrays exposed to tungsten foil coated graphite pipe emitters. **G** – Single MPV unit, fins are used to increase effective emissivity via the blackbody effect.

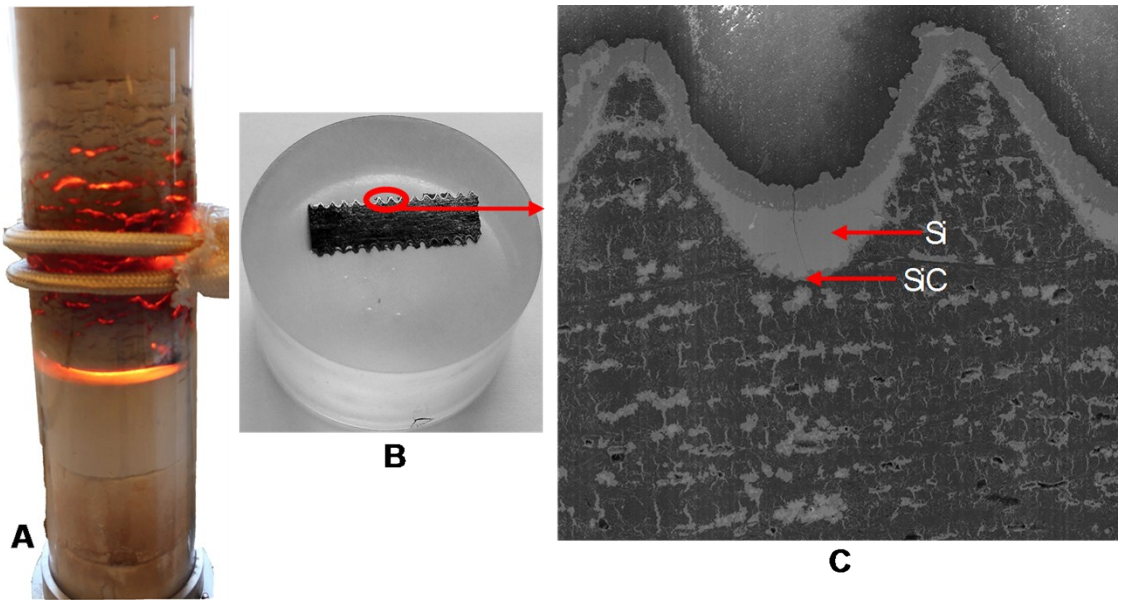

Extended Data Figure 7A – TEGS-MPV proof of concept scale experiment setup. **B** – Cross section of threaded rod after exposure to molten Si. **C** – SEM image of two teeth from the threaded rod showing SiC scale.

Mechanically, the tank wall thickness is designed to resist hoop stress with a minimum factor of safety (SF) of two, based on the tensile strength of isostatic graphite at room temperature (50 MPa), as shown in Equation 4. Here, t_g is the graphite thickness, ρ is the fluid density, g is the acceleration of gravity, H is the tank height, and r is the tank radius. This safety factor increases with temperature, as the graphite strength increases with temperature[33]. The hoop stress in the wall decreases linearly with height, as the internal pressure arises from the gravitational force acting on the fluid, and this fact can be leveraged to reduce the graphite required by up to a factor of two.

$$t_g = \frac{(\rho g H) r}{(\sigma_{fracture} / SF)} \tag{4}$$

$$t_{ins} = r_i \times \exp\left(\frac{2\pi H k (T_i - T_o)}{Q}\right) \tag{5}$$

The graphite tank is insulated with multiple layers of insulation, with the insulation thickness calculated using Equation 5 and the effective thermal conductivities listed in Extended Data Table 1. Here, r_i is the inner radius of the insulation layer, H is the tank height, k is thermal conductivity, $(T_i - T_o)$ is the temperature decrease across the layer, and Q is the heat loss. Immediately outside the graphite tank is graphite felt insulation, at a cost of \$7,000/m^3 based on multiple quotes. This material is used until the temperature decreases to 1,350°C. At this point, a lower cost aluminum silicate ceramic fiber blanket is used at a cost of \$400/m^3. The cost of this material is low in part because it is widely used in ovens. Even lower in cost and thermal conductivity is fiberglass insulation, at \$85/m^3, so this material is used as an outer insulation layer below 540°C. The insulation cost is dominated by the graphite felt layer, which bridges a 1,000°C

temperature decrease in the hot tank, but only 550°C in the cold tank. For this reason, the cold tank cost is $10/kWh-e cheaper than the hot tank.

The graphite tanks rest directly on rigid graphite insulation board, at a cost of $13,000/m^3. Below 1,700°C, this board rests on a calcium aluminate based castable cement (WAM ALII HD), at a cost of $6,000/m^3. This material is used for its compressive strength in a cinder block geometry, and the cavities are filled with aluminum silicate insulation to minimize cost, radiative heat loss, and natural convection. The castable cement then rests on a concrete foundation that can be cooled by forced air or water, as is the case in current molten salt CSP plants[60]. The concrete cost is $200/m^3 and cooling cost is estimated $60/m^2 based on a designed heat flux of 400 W/m^2 and cost of recirculated cooling[61] of $80/kW. These tanks reside inside an inert atmosphere, achieved with a cold steel[62] shell.

Construction costs are estimated based on the cost of constructing molten salt CSP tanks[17], along with the cost to assemble additional components. For example, the cost to layout and bolt together the graphite tanks is estimated assuming that each section takes five minutes to position and one minute to install each bolt. With an estimated worker salary of $50,000 per year, the total tank construction cost is to $3.14/kWh-e.

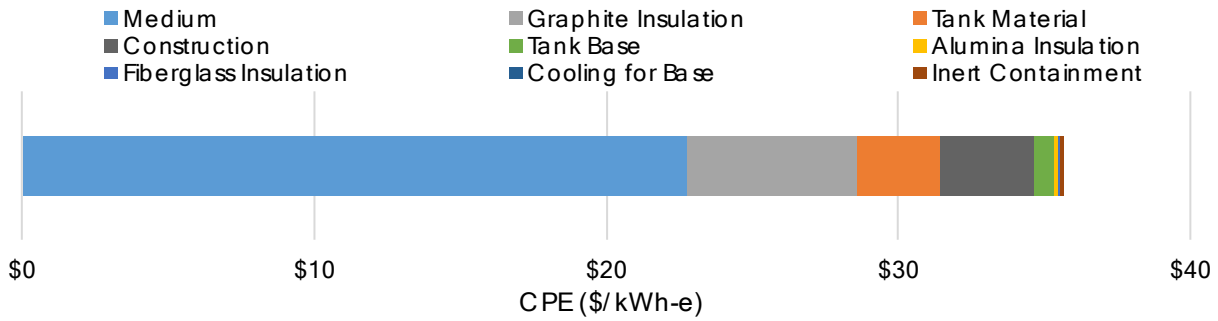

Extended Data Figure 8 – Tank cost breakdown for 100% Si medium base case

Heater

The heater consists of a 37 x 15 array of graphite pipes of 10 mm inner diameter and 20 mm outer diameter. Between columns of these pipes are graphite rods that are used as electric resistance heating elements as shown in Extended Data Figure 6F. The heater is designed so that the peak heater temperature is 2500°C. The pricing for pipes and rods is from graphitestore.com, at $100/m for pipes and $18/m for rods. A quote was obtained for these custom headers, at a cost of $0.25/kW. Thyristor based power supplies for the heaters were quoted at $5/kW. These supplies use silicon controlled rectifiers (SCR) to modulate power by rapidly switching, with efficiencies as high as 99.5%[34]. In a large heater such as this one, heating elements can be arranged in a series-parallel configuration to match the overall heater resistance to supplied voltage, thus reducing or eliminating the need for voltage transformers. The heater is insulated using the same approach as the tanks, by restraining the heat flux loss to be the same 400 W/m^2 as the tanks. The total heater cost is only $0.02/W-e because it is so power dense and is driven by the power supply cost, pipe cost, and heating element cost. A breakdown of the heater cost is given in Extended Data Figure 9.

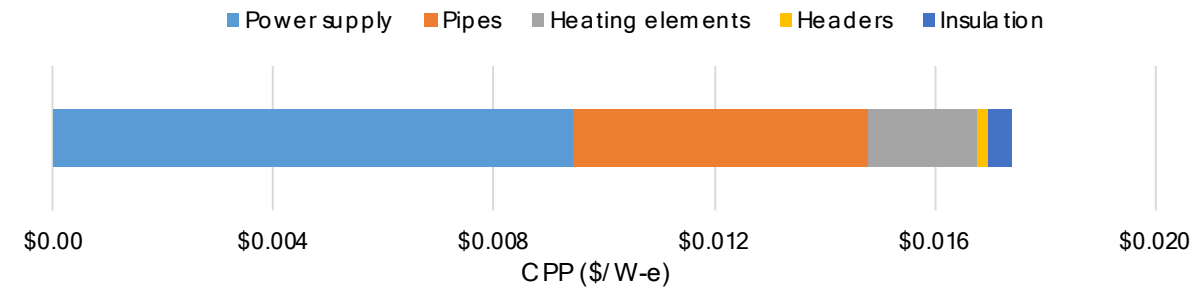

Extended Data Figure 9 – Heater cost breakdown for the base case

MPV Cost

The major variable in the power block cost is the MPV cell cost. It is expected that this cost will fall between the price of silicon PV cells[1] at $50/m^2 and the current cost of manufacturing GaAs cells at $10,000/m^2. The power density of this high temperature system is assumed to be 100 kW/m^2, resulting in a cell cost between $0.0005/W-e and $0.10/W-e. Nonetheless, here we have taken the more conservative upper limit on cost and lower limit on power density in our primary cost model. Another important cost is that of the inverters to convert the DC power to AC. These are priced at $0.08/W-e based on national averages[1] for central inverters in utility scale PV. Cooling of the MPV cells is estimated at $0.08/W based[61] on recirculating cooling 8°C above ambient, where the required cooling power per unit of electrical power generated is calculated as (1-RTE)/RTE. The numerator of this equation accounts for the waste heat generated, while the denominator normalizes it to electricity output, rather than heat input. W foil, which is used as a vapor pressure barrier to suppress the evaporation of graphite infrastructure was quoted at $700/m^2, or $0.035/W-e. The graphite piping and insulation is similar to the previously described systems and has a small effect on cost. The cost of constructing the MPV power block and heater are estimated by including other CPP construction costs based on previous analysis and adding the estimated labor cost to assemble additional components. For example, the time to install each pipe in the heater and MPV systems is estimated to be 10 minutes, and 30 minutes is estimated to install each unit of tungsten foil. Based on the labor rates discussed above, the construction cost of components that scale with power is estimated at $0.03/W-e. A breakdown of the MPV costs is given in Extended Data Figure 10. An overview and detail view of the MPV layout is shown in Extended Data Figure 6F and G.

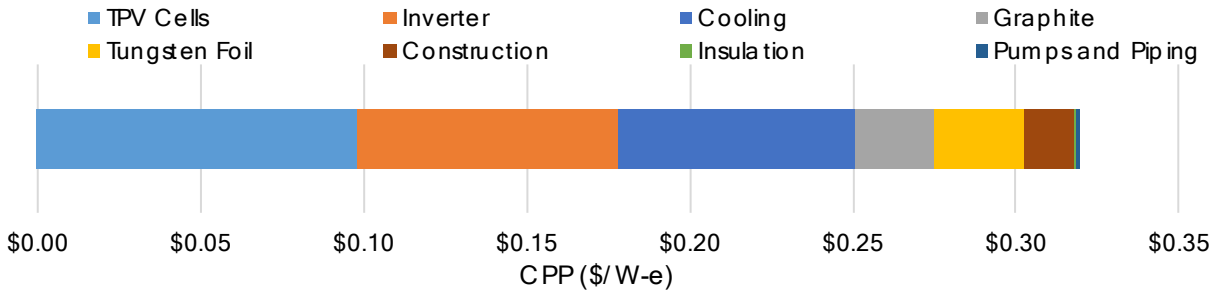

Extended Data Figure 10 – MPV cost breakdown for the base case

Pumps and piping

Because of the energy density of silicon, to discharge at 100MW-e, a flow rate of only 0.2 m^3/s (~3200 gpm) is needed. For perspective, this is similar in size to the water pumps found on fire engines. The pressure required is mostly to make up for gravitational head and will vary between 0.1-0.4 MPa (1-4 atm), which can easily be met with a centrifugal pump consuming ~ 40 kW of power. This flow rate and pressure can be met with a 330 mm (~ 1 ft) diameter centrifugal pump (SAE size 8x10-13), and the power requirement is negligible compared to the 100 MW-e power output, which a key advantage of using liquid Si/metal. The pump material is graphite, and the cost will be dominated by the 15 m shaft required to locate the pump in the bottom of the tank with the motor above the tank. The total mass of a pump is estimated at 2,000 kg and a pump is needed for each of the two tanks. The primary piping network between the tanks, heater, and MPV have a nominal diameter of 250 mm to minimize dynamic head loss. The cost of pumps and piping are included with components that scale with the power output (CPP) of the system and are shown in Extended Data Figure 10.

Extended Data Table 1: Material Costs and Properties

Material	Density (kg/m3)	Cost ($/kg)	Thermal Conductivity (W/m-K)	Temperature Limit (°C)	Source
553 Silicon	2400	1.6	25	3250	Quotes[63]
Isostatic Graphite	1850	7.0	30	3600	Quotes
Rigid Graphite Insulation	24	540	0.3	2800	Quotes[64]
Graphite Felt	14	500	0.3	2800	Quotes[64]
Aluminum Silicate	100	4.0	0.2	1350	Quotes[65]
Fiberglass Blanket	12	7.1	0.05	540	[66]
WAM ALII	2700	2.2	1.5	1700	Quotes[67]
Scrap steel	7000	0.1	30	2862	[68]
Tungsten Foil (0.1mm thick)	19000	350	100	3400	Quotes

Extended Data Table 2: Effect of IRR on Max CPP

					Max CPP			
	CPE	RTE	CPP	Life	0%	4%	15%	20%
TEGS-MPV	$36	50%	$0.34	30	$3.06	$1.62	$0.37	$0.18
PHS	$60	90%	$0.75	30	$4.90	$2.60	$0.61	$0.31
CAES	$27	75%	$0.60	30	$4.46	$2.49	$0.77	$0.52
Li-ion	$150	90%	$0.08	10	$0.33	$0.01	-$0.55	-$0.71
Lead-acid	$300	80%	$0.45	10	-$1.34	-$1.63	-$2.14	-$2.28
Flywheel	$2900	60%	$0.30	30	-$25.03	-$26.69	-$28.13	-$28.34

Alternative embodiments: Using solid storage

The usage of a liquid storage medium requires pumping, which could potentially be avoided if a solid storage medium were used. However, in the preceding analysis, we have focused specifically on liquids/metals because of the heat transfer issues that would arise from using a solid storage medium. It should also be noted that, in general, a gaseous storage medium will not have sufficiently high energy density to offer a competitive embodiment, since the density of gases is generally 2-3 orders of magnitude lower than that of a solid or liquid. This generalization assumes the gas is nominally at 1 atm pressure, such that any vessel used to contain it need not become a pressure vessel, which would become extremely thick walled and cost prohibitive at the large grid scales of interest. This generalization also assumes the gaseous medium's energy content is based on its sensible heat and not a chemical reaction enthalpy.

Then, to avoid pumping and enable storage in low cost solids, one may consider a solid medium. In this sense the idea is then to have a solid medium that consists of large blocks or alternative shapes and a key parameter becomes the surface area to volume ratio for the units of solid. Using graphite as an example solid, assuming a 500°C temperature swing (i.e., 1900-2400°C) with a nominal heat capacity of 1800 J kg^{-1} K^{-1}, density of 1800 kg/m^3 and a high temperature thermal conductivity of ~ 30 W m^{-1} K^{-1}, a 100 MW-e plant with 10 hrs of storage would require storage of 10^7 kg of graphite. This could be stored in a roughly 18 m diameter 18 m tall cylindrical tank and if the MPV power density was ~100 kW/m^2 as has been required herein to reach the high efficiencies that enable the concept to compete with PH, then ~ 1000 m^2 of surface area would be required. This may only require a small number (i.e., order 10) divisions of the graphite mass to make slots to insert the MPV cells. This is important, because it establishes the characteristic length over which the heat would is conducted during discharge. Generally, for storage times of 10 hrs or greater this characteristic length is greater than 1 ft, which is a key problem with such an approach. That is, inherently, the heat must be conducted from the body of the graphite to the surface where the radiation occurs. This is unavoidable in a situation where sensible heat is being used and the medium is stationary. Nonetheless, the order 100 kW/m^2 fluxes required to make the system efficient and cost effective will induce very significant thermal gradients and also thermal transients in the solid mass, especially near the surfaces.

For example, consider a solid block of graphite with an initially uniform temperature of 2400°C. If it is exposed to MPV cells that draw 100 kW/m^2, the surface will immediately cool as heat is conducted from the hotter portion of the block to the surface. In this case it is useful to estimate the temperature gradients that would develop, as well as the thermal transients since every material has intrinsic limits beyond which it will mechanically fracture and break into pieces. Conceptually, a mechanical fracture in such a system could prove catastrophic as a failure mechanism because it could cause a portion of the solid to fall or slide by gravity and directly contact an MPV cell, which would cause MPV failure and also presumably some melting. Nonetheless, the likelihood of such a failure can be assessed by approximating the solid block temperature profile as similar to that of a 1-D semi-infinite medium, for which a closed form solution exists[69] when there is a constant heat flux at the surface,

$$T(x,t) = T_i + \left(\frac{2q\sqrt{\alpha t/\pi}}{k}\right) exp\left(\frac{-x^2}{4\alpha t}\right) - \left(\frac{qx}{k}\right) erfc\left(\frac{x}{2\sqrt{\alpha t}}\right) \quad (6)$$

Where T_i is the initial temperature, q is the 100 kW/m^2 constant heat flux, α is the thermal diffusivity, k is the thermal conductivity, t is time and x is the depth being evaluated (i.e., the distance to the surface). Using the properties for graphite mentioned above, this simple calculation reveals that, for example at a location 1 cm deep from the surface, the temperature will decrease at a rate greater than 40°C/sec throughout the first two minutes of discharge. Such an extreme transient would surely result in cracking and mechanical failure within 100 cycles (based on our own previous experiments [unpublished] thermal cycling and cracking graphite with 100°C/min heating rates). Furthermore, a large thermal gradient of ~ 3300K/m would need to exist at the surface. Such a high gradient is not problematic for a thin walled pipe, as would also occur in the liquid based TEGS-MPV embodiment discussed herein. This is because, for example, a 5 mm thick pipe wall would only experience a 15-20°C temperature drop across its wall. However, a solid storage medium would have to have a low surface area to volume ratio to keep the MPV cost from dramatically increasing, and for a characteristic length of ~ 1 ft, the temperature difference would need to be ~ 1000°C. Such a large temperature difference is problematic from an efficiency standpoint because the surface would have to be ~1000°C colder than the center of the storage medium during the majority of the discharge. This would then lead to a much lower efficiency than what has been predicted herein for emitter surface temperatures in the range of 1900-2400°C. It should be further noted that this issue of the transient buildup of conductive thermal resistance during discharge is rather fundamental and immutable. It is an intrinsic characteristic of relying on transient heat conduction through a solid for the discharge. Although the cost of solid storage media could potentially be very low, the thermal management issues that would arise during the discharge are daunting, and possibly insurmountable. It is for this reason that a liquid storage medium is highly preferred and likely the only way to realize a system with sufficiently high efficiency that it can enable eventual 100% penetration of renewables.

References:

42 State of the Market Report for PJM. (Monitoring Analytics, LLC, 2015).

43 Serreze, H. B. Optimizing solar cell performance by simultaneous consideration of grid pattern design and interconnect configuration. *13th Photovoltaic Specialists Conference*, 609-614 (1978).

44 Friedman, D. J., Olson, J. M. & Kurtz, S. in *Handbook of Photovoltaic Science and Engineering* Ch. 8, (2011).

45 Ward, J. S. A novel design for monolithically interconnected modules (MIMs) for thermophotovoltaic (TPV) power conversion. *Proc. 3rd NREL Thermophotovoltaic Generation of Electricity Conf.*, 227-236 (1997).

46 García, I. *et al.* Metamorphic Ga0.76In0.24As/GaAs0.75Sb0.25 tunnel junctions grown on GaAs substrates. *Journal of Applied Physics* **116**, 074508, doi:10.1063/1.4892773 (2014).

47 Bedair, S. M. AlGaAs tunnel diode. *Journal of Applied Physics* **50**, 7267-7268, doi:10.1063/1.325809 (1979).

48 Barrigón, E., García, I., Barrutia, L., Rey-Stolle, I. & Algora, C. Highly conductive p + + -AlGaAs/n + + -GaInP tunnel junctions for ultra-high concentrator solar cells. *Progress in Photovoltaics: Research and Applications* **22**, 399-404, doi:10.1002/pip.2476 (2014).

49 Dimroth, F., Beckert, R., Meusel, M., Schubert, U. & Bett, A. W. Metamorphic GayIn1−yP/Ga1−xInxAs tandem solar cells for space and for terrestrial concentrator applications at C > 1000 suns. *Progress in Photovoltaics: Research and Applications* **9**, 165-178, doi:10.1002/pip.362 (2001).

50 Lumb, M. P. *et al.* Double quantum-well tunnel junctions with high peak tunnel currents and low absorption for InP multi-junction solar cells. *Applied Physics Letters* **100**, 213907, doi:10.1063/1.4722890 (2012).

51 France, R. M. *et al.* Quadruple-Junction Inverted Metamorphic Concentrator Devices. *IEEE Journal of Photovoltaics* **5**, 432-437, doi:10.1109/JPHOTOV.2014.2364132 (2015).

52 Geisz, J. F. *et al.* 40.8% efficient inverted triple-junction solar cell with two independently metamorphic junctions. *Applied Physics Letters* **93**, 123505, doi:10.1063/1.2988497 (2008).

53 France, R. M., McMahon, W. E., Norman, A. G., Geisz, J. F. & Romero, M. J. Control of misfit dislocation glide plane distribution during strain relaxation of CuPt-ordered GaInAs and GaInP. *Journal of Applied Physics* **112** (2012).

54 McMahon, W. E. *et al.* Dislocation Glide Enhancement in Ordered III-V Alloys. *Journal of Applied Physics* **114** (2013).

55 France, R. M. *et al.* Quadruple Junction Inverted Metamorphic Concentrator Devices. *Journal of Photovoltaics* **5**, 432-437 (2015).

56 France, R. M. *et al.* Lattice-Mismatched 0.7 eV GaInAs Solar Cells Grown on GaAs Using GaInP Compositionally Graded Buffers. *Journal of Photovoltaics* **4**, 190-195 (2014).

57 Patel, P. *et al.* Experimental Results From Performance Improvement and Radiation Hardening of Inverted Metamorphic Multijunction Solar Cells. *IEEE Journal of Photovoltaics* **2**, 377-381, doi:10.1109/JPHOTOV.2012.2198048 (2012).

58 Stan, M. *et al.* High-efficiency quadruple junction solar cells using OMVPE with inverted metamorphic device structures. *Journal of Crystal Growth* **312**, 1370-1374, doi:https://doi.org/10.1016/j.jcrysgro.2009.10.059 (2010).

59 Ray Martyn, S. Thermal Radiation Heat Transfer, 3rd edn, by R. Siegel and J.R. Howell, Hemisphere Publishing Corporation, USA (1992). 1072 pages. ISBN 0-89116-271-2. *Developments in Chemical Engineering and Mineral Processing* **2**, 190-190, doi:10.1002/apj.5500020220 (1994).

60 Gabbrielli, R. & Zamparelli, C. Optimal Design of a Molten Salt Thermal Storage Tank for Parabolic Trough Solar Power Plants. *Journal of Solar Energy Engineering* **131**, 041001-041001-041010, doi:10.1115/1.3197585 (2009).
61 Zhai, H. & Rubin, E. S. Performance and cost of wet and dry cooling systems for pulverized coal power plants with and without carbon capture and storage. *Energy Policy* **38**, 5653-5660, doi:https://doi.org/10.1016/j.enpol.2010.05.013 (2010).
62 Wilk, G. *Liquid metal based high temperature concentrated solar power: Cost considerations* M.S. thesis, Georgia Institute of Technology, (2016).
63 Endo, R., Fujihara, Y. & Susa, M. *Calculation of the density and heat capacity of silicon by molecular dynamics simulation*. Vol. 35/36, doi:10.1068/htjr135 (2003).
64 *Carbon Fiber Products - Soft felt*, <http://www.carbon.co.jp/english/products/fine_carbon/> (
65 *Alumina-Silica Blanket - Type ASB*, <https://www.zircarceramics.com/product/asb/> (
66 Smith, D. R., Hust, J. G. & Poolen, L. J. V. Effective Thermal Conductivity of a glass fiberblanket standard reference material. Report No. NBSIR 81-1640, (Thermophysical Properties Division, National Engineering Laboratory, National Bureau of Standards, 1981).
67 *ALII Products*, <http://westadmat.com/aliiproducts/> (
68 Nishi, T., Shibata, H., Waseda, Y. & Ohta, H. Thermal conductivities of molten iron, cobalt, and nickel by laser flash method. *Metallurgical and Materials Transactions A* **34**, 2801-2807, doi:10.1007/s11661-003-0181-2 (2003).
69 Bergman, T. L., Lavine, A. S., Incropera, F. P. & DeWitt, D. P. *Fundamentals of Heat and Mass Transfer*. (Wiley, 2016).